Petroleum Science 20 (2023) 3567–3581

Contents lists available at ScienceDirect

Petroleum Science

journal homepage: www.keaipublishing.com/en/journals/petroleum-science

Original Paper

Numerical study of hydraulic fracturing in the sectorial well-factory considering well interference and stress shadowing

Yu-Hao Liu [a, b], Jin-Tao Zhang [c], Jie Bai [d], Feng-Shou Zhang [a, b, *], Ji-Zhou Tang [e, f]

[a] Key Laboratory of Geotechnical & Underground Engineering of Ministry of Education, Tongji University, Shanghai, 200092, China
[b] Department of Geotechnical Engineering, College of Civil Engineering, Tongji University, Shanghai, 200092, China
[c] Southwest Oil & Gas Field Company, PetroChina, Chengdu, 610017, Sichuan, China
[d] Oil and Gas Technology Research Institute, PetroChina Changqing Oilfield Company, Xi'an, 710021, Shaanxi, China
[e] National Key Laboratory of Marine Geology, Tongji University, Shanghai, 200092, China
[f] School of Ocean and Earth Science, Tongji University, Shanghai, 200092, China

ARTICLE INFO

Article history:
Received 25 November 2022
Received in revised form
24 May 2023
Accepted 28 May 2023
Available online 29 May 2023

Edited by Yan-Hua Sun

Keywords:
Hydraulic fracturing
Sectorial well-factory
Fracture deflection
Well interference
Stress shadowing

ABSTRACT

In the Changqing Oilfield in northwest China, when traditional petroleum exploitation encounters forestry reserves or water source protection areas, sectorial well-factory design is proposed. The most distinct feature of a sectorial well-factory is the deviation of the well from the minimum horizontal principal stress, resulting in hydraulic fracture deflection after the initiation, along with possible well interference (i.e., fracture hit) and fracture coalescence in the oblique wells. Four indexes describing well deflection are then proposed according to fracture morphology. Several fracturing designs, including stage arrangement, fracturing sequences, and fracturing techniques are applied to study the feasibility of the sectorial well-factory design. The results show that the "gradual" or "sparse" stage arrangement, large injection rate, and simultaneous multifracture treatment can help to optimize the fracture morphology and stimulation design. However, the subsequent stress shadowing effect usually adversely affects the fracturing of adjacent wells. With a small initial horizontal stress difference, large injection rate and staggered stage arrangement can achieve ideal stimulation performance. Our results can provide a guidance for optimizing stimulation design in unconventional well-factory while taking into account environmental protection.

1. Introduction

Hydraulic fracturing is a widely used artificial stimulation technique for commercial exploitation in unconventional reservoirs with low porosity and low permeability. A large number of practices and studies have proved that staged multi-cluster fracturing from multiple well pads is a key technique to further reduce treatment costs and improve fracturing performance. The common approach is the parallel well-factory, in which all horizontal wells are drilled along the optimal orientation, i.e., the direction of the minimum horizontal principal stress (S_{hmin}) as shown in Fig. 1(a). As a result, hydraulic fractures propagate perpendicular to the wellbore through massive fluid injection, eventually achieving the efficient stimulation of the target reservoir in a certain direction. Numerous studies have been carried out to investigate the propagation and interaction behavior of hydraulic fractures in multiple parallel horizontal wells during the staged multi-cluster fracturing. For the calculation of fracture size during multifracture treatment analytical methods have not made much progress because it is more complex than the propagation of single and regular fracture. Only some analytical solutions were developed to assess the results of well interference, including the degree of fracture hit (Molina and Zeidouni, 2017), rate transient data (Liu Q. et al, 2020; Thompson, 2018; Wei et al., 2022) and the location of observation wells (Al-Khamis et al., 2003). Advanced numerical simulations can overcome the lack of analytical methods to present complex fracture morphology at engineering scale with field data. For the planar fracture model, embedded discrete fracture model (EDFM) is a popular method to simulate the impact of well interference (Tang et al., 2017; Yu et al., 2017, 2018) and it can be combined with a

* Corresponding author. Key Laboratory of Geotechnical & Underground Engineering of Ministry of Education, Tongji University, Shanghai, 200092, China.
E-mail address: fengshou.zhang@tongji.edu.cn (F.-S. Zhang).

https://doi.org/10.1016/j.petsci.2023.05.020

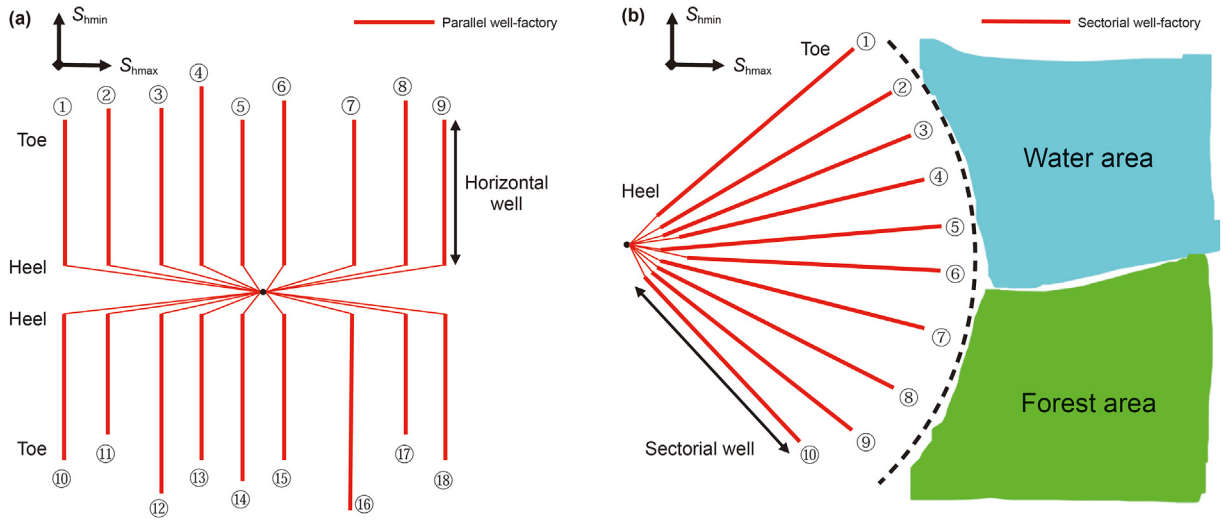

Fig. 1. Schematic diagram of (**a**) parallel well-factory, and (**b**) sectorial well-factory.

commercial black oil reservoir simulator for multi-well history matching (Xavier Fiallos et al., 2019). For the nonplanar fracture model, Wu and his coworkers (Wu and Olson, 2015, 2016; Wu et al., 2018) analyzed the dynamic-stress evolution and multiple-fracture propagation in horizontal wells through a simplified three-dimensional (3D) displacement discontinuity method (DDM). Discrete element method (DEM) is also applied to simulate different completion designs for simultaneous fracturing from two horizontal wells (Duan et al., 2021). Furthermore, DEM can be coupled with hydromechanics to consider the nonplanar 3D growth of hydraulic fractures in layered reservoirs (Yang et al., 2016). As for the design of fracturing strategy, many studies have investigated the influence of well interference under different fracturing techniques and confirmed that zipper fracturing yields better well performance (Chen et al., 2018; Sobhaniaragh et al., 2017; Wang Z. et al., 2022; Feng et al., 2016, 2017; Vidma et al., 2018; Yoshioka et al., 2021; Zhao et al., 2022). Through numerical simulations and experiment studies, stress shadowing effect have been investigated during hydraulic fracturing in horizontal wells (Daneshy et al., 2012; Liu X. et al., 2020; Shan et al., 2021; Wang L. et al., 2022; Wang X. et al., 2022a, 2022b, 2022c; Bourdin et al., 2012; Tang J. et al., 2019; Tang X. et al., 2019).

The aforementioned studies are all based on the scenario of parallel well-factory but cannot provide guidance for some special well patterns. In the exploitation of unconventional reservoirs, environmentally sensitive areas such as forestry reserves and water source protection zones are sometimes encountered. In this case, it is difficult to drill traditional parallel wells, resulting in a rather inadequate stimulation of the target reservoirs. Fig. 1(b) is an example of a pad layout based on environmental protection in the Changqing Oilfield in northwest China. A sectorial well-factory layout is designed to avoid surface operations while recovering the underlying reservoir. In this complex well pattern, the azimuth of each horizontal well deviates from the optimal orientation at different angles, and the spacing between wellbores increases from heel to toe, resulting in complex propagation behavior of hydraulic fractures. To date, limited studies have focused on the dynamic growth of hydraulic fractures in oblique horizontal wells. The determination of the optimal well azimuth is mainly based on field data (LaFollette and Holcomb, 2011; Zinn et al., 2011). Studies have shown that the more the horizontal wellbore deviates from the minimum horizontal stress, the lower the estimated ultimate recovery. Wang et al. (2023), Wutherich et al. (2013) and Yang et al. (2016) carried out numerical studies on fracturing at different drilling azimuths, which were mostly focused on production comparison. In summary, extremely limited effort has been reported in studying fracturing in sectorial well-factory. The fracture propagation behavior and stress shadowing evolution between multiple clusters and multiple non-parallel horizontal wells remain unclear.

In this study, we develop a three-dimensional (3D) lattice method based model for staged multi-cluster fracturing for the sectorial well-factory to explore the feasibility of hydraulic fracturing considering well interference and stress shadowing. All the wells in the model are set deviated from the optimal orientation at different angles and some evaluation indexes are proposed based on the analysis of fracture deflection behavior from a single stage. With these indexes fracture propagation under different stage arrangements, fracturing sequences and fracturing techniques are discussed scientifically to conclude the characteristic of well interference and stress shadowing in oblique horizontal wells. Our research results can provide a guidance for fracturing optimization design in unconventional well-factory under environmental protection requirements.

2. Numerical method of discrete lattice

XSite, a numerical code based on synthetic rock mass and lattice method, has been used to simulate the propagation behavior of hydraulic fractures in fractured rocks (Damjanac and Cundall, 2016; Damjanac et al., 2016; Bakhshi et al., 2019; Benouadah et al., 2021; Detournay et al., 2022). Developed as a simplified version of the particle flow code (PFC) utilizing the bonded particle model (BPM), the main advantage of the lattice approximation is its computational performance by loss of generality. Lattice approximation is achieved by discretizing the porous medium into mass nodes with springs, as shown in Fig. 2(a), which represent particles and contacts. Each fluid node is located in the center of the spring, and fluid flows between the pipes connecting the fluid nodes.

2.1. Mechanical model

There are three translations and three rotations for each node in the lattice. The explicit solution scheme is ideal for directly

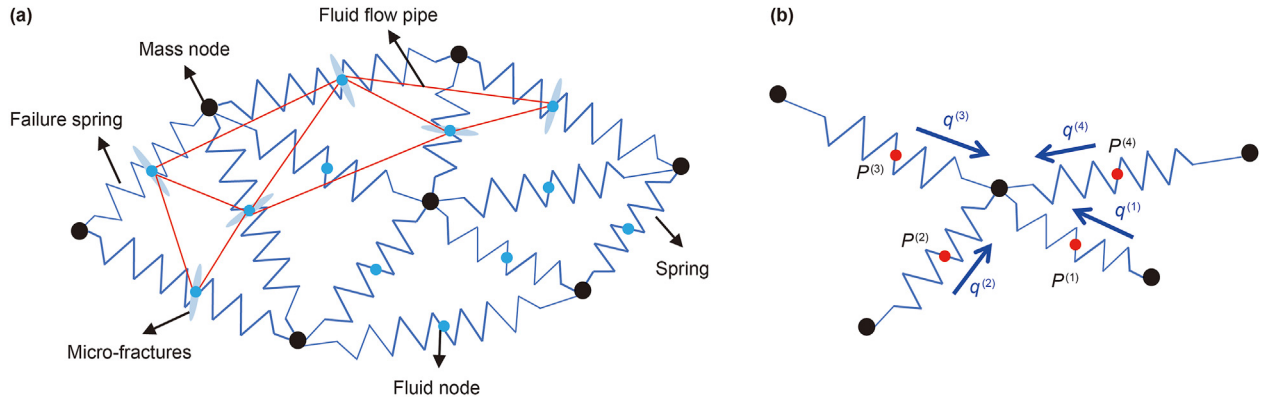

Fig. 2. (**a**) Lattice approximation in XSite, (**b**) fluid variables in the matrix flow. Red dots represent spring pressures and blue arrows represent fluid flow along the springs.

simulating highly nonlinear behavior such as propagation, slippage, and failure of joints. The following set of central difference formulas controls the motion of each node (Damjanac et al., 2016; Damjanac and Cundall, 2016):

$$\begin{cases} \dot{u}_i^{(t+\Delta t/2)} = \dot{u}_i^{(t-\Delta t/2)} + \sum F_i^{(t)} \Delta t \big/ m \\ u_i^{(t+\Delta t)} = u_i^{(t)} + \dot{u}_i^{(t+\Delta t/2)} \Delta t \end{cases} \tag{1}$$

where $u_t^{(i)}$ is the position of component i (i = 1–3) and $\dot{u}_t^{(i)}$ represents the corresponding velocity of component i (i = 1–3) at time t; $\sum F_i^{(t)}$ is the total force acting on the mass m at time t; Δt represents the time step. The angular velocity is calculated by the following equation:

$$w_i^{(t+\Delta t/2)} = w_i^{(t-\Delta t/2)} + \frac{\sum M_i^{(t)}}{I} \Delta t \tag{2}$$

where $\sum M_i^{(t)}$ is the total moment of component i (i = 1–3) and I represents the moment of inertia.

For an intact spring, the relative velocity between node A and node B can be written as:

$$\dot{u}_i^{\mathrm{rel}} = \dot{u}_i^{\mathrm{A}} - \dot{u}_i^{\mathrm{B}} \tag{3}$$

then the normal and tangential velocities can be calculated as:

$$\begin{cases} \dot{u}_i^{\mathrm{N}} = \dot{u}_i^{\mathrm{rel}} n_i \\ \dot{u}_i^{\mathrm{S}} = \dot{u}_i^{\mathrm{rel}} - \dot{u}_i^{\mathrm{N}} n_i \end{cases} \tag{4}$$

where N denotes “normal”; S denotes “shear”; n_i is the unit normal vector, and the Einstein summation convention applies to repeated indices. The normal stress and shear stress of the spring in the model can be calculated by the mutual displacement of nodes (Damjanac and Cundall, 2016; Damjanac et al., 2016) as:

$$\begin{cases} F_i^{\mathrm{N}} \leftarrow F_i^{\mathrm{N}} + \dot{u}_i^{\mathrm{N}} K^{\mathrm{N}} \Delta t \\ F_i^{\mathrm{S}} \leftarrow F_i^{\mathrm{S}} + \dot{u}_i^{\mathrm{S}} K^{\mathrm{S}} \Delta t \end{cases} \tag{5}$$

where K^{N} and K^{S} are the normal and shear stiffnesses of the spring, respectively. Here we assume that the normal stress is positive in tension. When the spring stress exceeds the predefined tensile or shear strength, the spring breaks and micro-fractures are generated with $F^{\mathrm{N}} = 0$ and $F^{\mathrm{S}} = 0$.

2.2. Flow model

XSite simulates single-phase fluid flow in both fractures and matrix while using different solutions. For fluid flow in fractures, it is solved in the network of fluid nodes and pipes as shown in Fig. 2(a), including initial fractures and subsequently generated micro-fractures. The flow in matrix is represented by the pore pressure in the spring of a lattice, which is related to permeability, fluid storage, and leak-off into the rock, and fluid can exchange between fractures and the matrix.

2.2.1. Fluid flow in fractures

As aforementioned, fracturing fluid flows along pipes connecting micro-fractures (or in initial fractures specified as model inputs in the cluster), which is described by the lubrication equation. Thus, the flow rate in the pipe connecting broken fluid nodes A and B is calculated as:

$$q = \beta k_{\mathrm{r}} \frac{a^3}{12\mu} \left[P^{\mathrm{A}} - P^{\mathrm{B}} + \rho_{\mathrm{w}} g \left(z^{\mathrm{A}} - z^{\mathrm{B}} \right) \right] \tag{6}$$

where β is a dimensionless calibration parameter; k_{r} is the relative permeability; a is the hydraulic aperture; μ is the fluid viscosity; P^{A} and P^{B} represent the fluid pressures at node A and node B, respectively; ρ_{w} is the fluid density; g is the acceleration of gravity; z^{A} and z^{B} represent the elevations of node A and node B, respectively.

Using the explicit numerical scheme again, the pressure increment ΔP in the evolution of the fracture flow during each time step Δt_{f} equals:

$$\Delta P = \frac{\sum q_i}{V} \overline{K}_{\mathrm{F}} \Delta t_{\mathrm{f}} \tag{7}$$

where $\overline{K}_{\mathrm{F}}$ is the apparent fluid bulk modulus; V is the node volume; $\sum q_i$ is the sum of all flow rates from the pipes connected to the fluid node.

2.2.2. Fluid flow in matrix

Fluid flow in matrix should be taken into consideration if leak-off is non-negligible, assuming that the fluid will penetrate into the intact rock. The matrix pressure is solved in the lattice spring, which only exists in the original lattice data structure in Fig. 2(b). Removing the pre-existing joints in the model, the pressure in the remaining springs of the rock matrix is equal to the matrix pressure. Therefore, the flow rate in the matrix can be calculated by the difference in local spring pressures:

$$q^{(i)} = \eta_i\left(P^{(i)} - \overline{P}\right) \tag{8}$$

where $q^{(i)}$ is the flow rate of the ith spring, η_i is the conductivity; and $\overline{P}$ is the "virtual" pressure at each node. Then the unbalance of two distinct flows within a spring defines the change in matrix pressure (Damjanac et al., 2016):

$$\Delta P^{(i)} = \left(q^{(i)}_{\text{left}} - q^{(i)}_{\text{right}}\right)k\Delta t_{\text{f}}\Big/A^2 \tag{9}$$

where $q^{(i)}_{\text{left}}$ and $q^{(i)}_{\text{right}}$ are the flow rates of left and right spring segments, respectively; k is the apparent mechanical stiffness of the fluid node; Δt_{f} is the fluid time step; and A is the apparent spring area.

2.3. Hydromechanical coupling

The mechanical model and the flow model are fully coupled by an efficient sequential explicit calculation method of the 3D discrete lattice method (Damjanac et al., 2016; Damjanac and Cundall, 2016; Bakhshi et al., 2019). There are three aspects of hydro-mechanical coupling presented in the following.

(1) Fracture permeability depends on the initial aperture and rock deformation. In Eq. (6) the cubic law provides a relationship between the flow rate and hydraulic aperture where fracture permeability k_{f} is calculated as:

$$k_{\text{f}} = \frac{a^2}{12} \tag{10}$$

(2) Fluid pressure affects rock deformation and strength. The effective stress calculations are carried out.

(3) Rock deformation in turn leads to changes in fluid pressure. Eq. (7) presents the pressure increment and the apparent fluid bulk modulus $\overline{K}_{\text{F}}$ is calculated by hydraulic aperture a and the apparent spring area A when one-dimensional fluid stiffness is much larger than the rock stiffness:

$$\overline{K}_{\text{F}} = \frac{a}{A}\left(k_{\text{R}} + k_{\text{J}}\right) \tag{11}$$

where k_{R} and k_{J} represent the one-dimensional rock stiffness and joint stiffness, respectively.

3. Model verification

We verify the numerical model based on the propagation of a 3D penny-shaped fracture in a toughness dominated regime without considering leak-off. According to the geological and engineering parameters in Table 1, we compare the geometric dimensions of the 3D penny-shaped fracture obtained by numerical simulation and theoretical solution (Dontsov, 2016, 2022; Detournay, 2016):

Table 1
Input parameters in the verification model.

Input parameter	Value
Young's modulus, GPa	10
Fracture toughness, Pa·m$^{0.5}$	1e7
Fluid viscosity, Pa·s	0.005
Carter's leak-off parameter, m/s$^{0.5}$	0
Poisson's ratio	0.26
Injection rate, m^3/s	0.02
Injection time, s	500

$$w_{\text{k}}\left(\frac{r_{\text{k}}(t)}{R_{\text{k}}(t)}, t\right) = 0.6537\left(\frac{K'^4 Q_0 t}{E'^4}\right)^{1/5}\left(1 - \left(\frac{r_{\text{k}}(t)}{R_{\text{k}}(t)}\right)^2\right)^{1/2} \tag{12}$$

$$R_{\text{k}}(t) = 0.8546\left(\frac{E' Q_0 t}{K'}\right)^{2/5} \tag{13}$$

Eq. (12) along with Eq. (13) describes the relationship of hydraulic aperture, w_{k}, and the fracture radius, r_{k}, with an injection rate, Q_0, in a total injection time, t, analytically. K' and E' are written in the scaled form to represent rock toughness and Young's modulus, respectively. Dontsov (2016) provided other details for the theoretical solution.

The fracture morphology obtained from numerical simulation is shown in Fig. 3(a). A circular penny-shaped fracture is formed in the domain. The size of the fracture obtained by the numerical simulation is in a good agreement with the theoretical solution, as shown in Fig. 3(b). The errors mainly occur at the center and the tips of the fracture. At small distances, the numerical injection source is a finite volume rather than a point source which is assumed in the theoretical solution. Therefore, the numerical fracture is narrower; at large distances, the exact solution assumes no seepage because of a zero initial aperture but the numerical solution allows seepage ahead of the fracture tip to obtain a larger fracture width than the theoretical solution. This is consistent with previous findings (Damjanac and Cundall, 2016; Damjanac et al., 2016). The above analysis clearly shows that the numerical model can characterize the hydraulic fracturing process well.

4. Fracture propagation in the sectorial well-factory

4.1. Simulation of fracture morphology

We built seven single-staged models named as Well 1-1 to Well 1-7 in Fig. 4. The wellbore azimuth of each horizontal well deviated from the direction of S_{hmin} varies from 0° to 90°. In each case, there is one single stage containing 3 clusters in the center of a 150 m × 150 m × 70 m region with a cluster spacing of 10 m. The initial horizontal stress difference between S_{hmax} and S_{hmin} is 5 MPa. Other input parameters are the same as listed in Table 2. It should be noted that we do not consider the small-scale fracturing behavior in the near-wellbore area, and only focus on the macroscopic propagation behavior of hydraulic fractures on the wellbore scale. Therefore, it is assumed that the initial disc-shaped fracture is perpendicular to the wellbore, instead of the actual perforation cluster. The sizes of the initial preset fractures and clusters are on a scale comparable to the wellbore for computational efficiency, which may deviate from reality but can be accepted for field-scale problems. All the following numerical examples in this paper are based on this assumption.

The results of fracture morphology of each non-parallel horizontal well are displayed in Fig. 4(a). It is expected that fractures will propagate along the pre-existing fractures perpendicular to the horizontal wellbore in the optimal azimuth. As the azimuth of the wellbore increases from the direction of S_{hmin}, fracture coalescence between clusters starts to occur. After the initiation, hydraulic fractures will reorient to the direction of S_{hmax}, governed by the stress differential. In the extreme situation where the deviated angle is close to 90°, fractures deflect to the wellbore azimuth and bifurcate during fracturing. Notably, in Well 1-7, the middle fracture in the stage propagates perpendicular to the wellbore, which may be caused by the stress shadowing of the fractures at both ends.

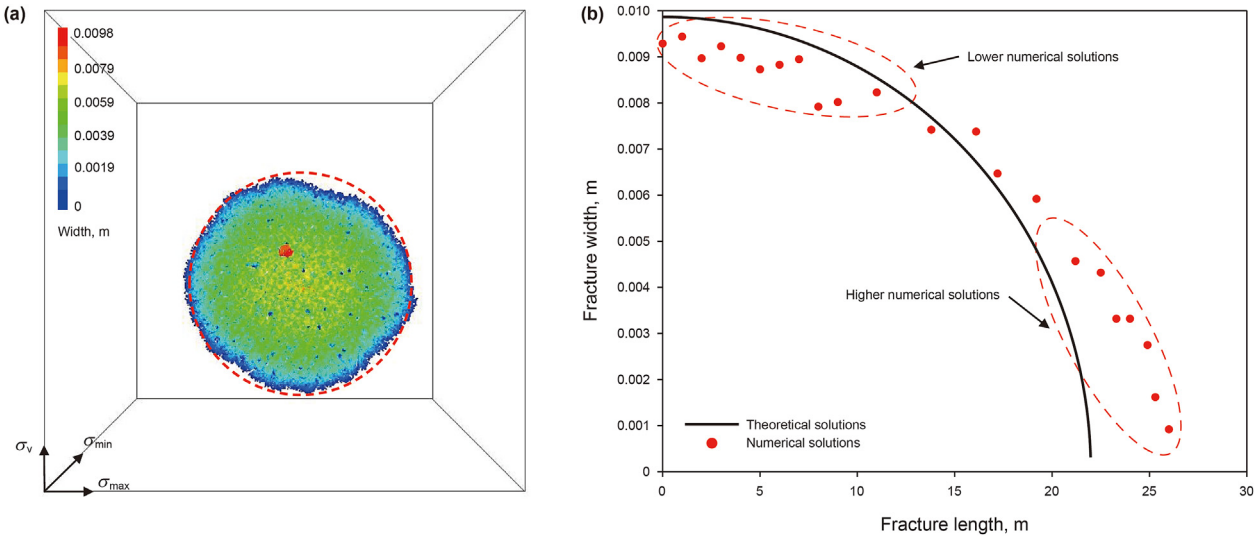

Fig. 3. (**a**) Fracture morphology obtained from numerical simulation, (**b**) comparison of geometric dimensions between numerical and theoretical solutions.

4.2. Evaluation indexes for the sectorial well-factory

Fig. 5 shows schematic diagrams of the fracture morphology of the sectorial well-factory based on the numerical results of Section 4.1. In Fig. 5(a), fracture deflection refers to the reorientation behavior of hydraulic fracture from the preset direction to the S_{hmax} direction under the impact of the horizontal principal stresses. We use a straight line to connect the initial point *O* with point *C* of the hydraulic fracture tip, and then draw a straight line perpendicular to the horizontal wellbore from point *C* to point *B*. We then draw a straight line from point *O* perpendicular to the horizontal wellbore, which is denoted as *OA*. In Fig. 5(b), the orange and red circles represent fracture coalescence, and the blue circle represents well interference. Based on previous studies, fracture coalescence between clusters and stages correlates positively with the formation of a complex fracture network, so we only regard well interference between wells as unfavorable.

Therefore, two characteristics of fracture propagation in the sectorial well-factory are well interference and fracture deflection. Based on the above concepts, we propose four evaluation indexes:

- Well interference between wells.
- Deflection distance, i.e., the length of line segment *BC*.
- Deflection angle, i.e., $\angle AOC$, which is defined as:

$$\alpha = 90 - \arctan\frac{BC}{OB} \tag{14}$$

where *BC* and *OB* are the lengths of the segments *BC* and *OB*, respectively.

Note that only the deflection distance and fracture angle at both ends are chosen in one stage to evaluate the entire fracture morphology.

- Covering area, defined as the sweep area of the hydraulic fracture:

$$S = S_{polygon} \tag{15}$$

where $S_{polygon}$ is the area of the domain covered by the final complex fracture network, as shown in Fig. 5(b).

5. Numerical simulations for fracture optimization

In this section, various possible optimization designs are tested in the numerical model, and the results are evaluated by using the proposed evaluation indexes.

5.1. Improved stage arrangement for a single well

We first consider improving the treatment performance for a single multi-staged non-parallel horizontal well in the sectorial well-factory. Based on the pad layout shown in Fig. 1(b), we design a target sectorial well-factory containing ten non-parallel horizontal wells, as shown in Fig. 6. The deviated angles between the direction of S_{hmin} are listed in Table 3. The ten wells are divided into two groups, conventional production wells and potential production wells. Wells with a deviated angle greater than 70° from the S_{hmin} are defined as conventional production wells, otherwise as potential production wells. The location of potential production wells is defined as an extreme region. Then Wells 2-1, 2-2, 2-3, 2-8, 2-9, and 2-10 of the ten wells are conventional production wells, and the remaining wells belong to potential production wells. Due to limited computational resource, only two fracturing stages per well with three clusters per stage are simulated in a 500 m × 300 m × 70 m domain. The geological and engineering parameters are provided in Table 4.

We start by considering the fracturing of three conventional production wells, Wells 2-1, 2-2, and 2-10. Due to the relatively small deviation angle and the decreasing wellbore spacing between two adjacent wells from toe to heel, we vary stage spacing and cluster spacing. The stages set in each well can be divided into two groups, as shown in Fig. 7. Group 1 is close to the heel and the stages have large cluster spacing and stage spacing, while Group 2 is close to toe, the cluster spacing and stage spacing are smaller. The specific values of cluster and stage spacing for each well are illustrated in the corresponding geometric models in Fig. 7. From the numerical results, due to the small deviation angle, the fracture deflection is small, and there are not many additional fracture branches. In addition, the fracture lengths are long enough to constitute a sufficiently large covering area of each well and the values are marked respectively near the red polygons. Therefore, the “gradual” stage arrangement for conventional production wells can achieve better treatment performance.

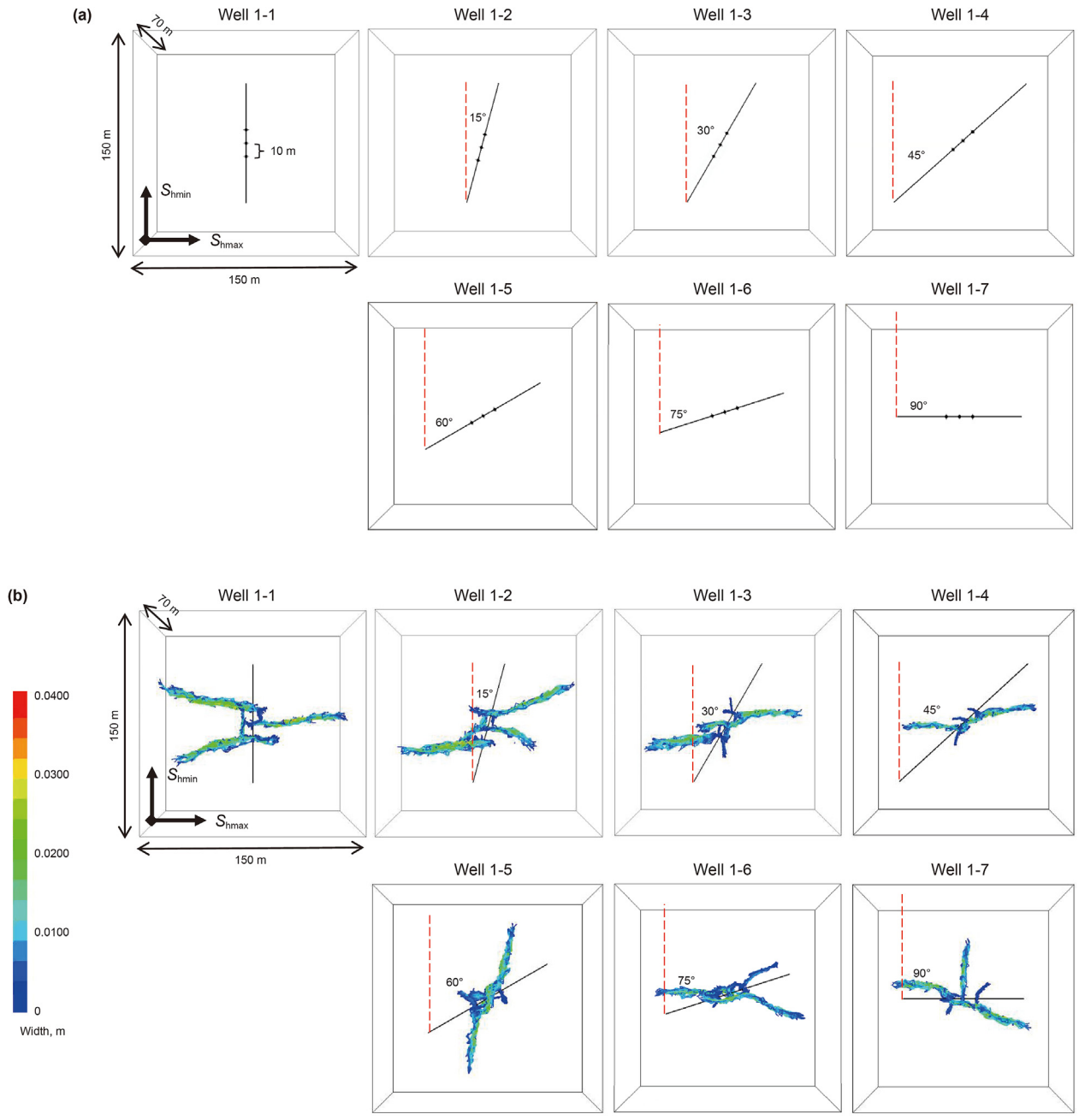

Fig. 4. (**a**) Schematic of the wells in the sectorial well-factory, (**b**) fracture morphology of each well at the end of injection.

Table 2
Input parameters for the single-staged models.

Input parameter	Value
Young's modulus, GPa	30
Fracture toughness, Pa·m$^{0.5}$	1e6
Poisson's ratio	0.25
Porosity, %	8.83
Permeability, mD	0.1
Injection rate, m^3/s	3
Injection time, s	900

For fracturing potential production wells, the same design as conventional production wells is first applied to arrange the stages for Well 2-4, as shown in Fig. 8(a). However, due to a large deviation angle, fractures deflect immediately after initiation, causing strong fracture coalescence connecting to the well. As a result, the coverage area of the fracture network is much smaller than the acceptable value. Therefore, as shown in Fig. 8(b), the stages are evenly placed along the wellbore with a larger cluster and stage spacing, which is defined as a "sparse" stage arrangement. Although the total number of hydraulic fractures in the same distance is reduced, simulation results show a larger coverage area. Potential production Wells 2-5 and 2-6 are also stimulated following the "sparse" stage arrangement strategy, and the corresponding fracture networks are shown in Fig. 9. Notably, the covering area of the potential production well is usually smaller than that of the conventional production well, indicating lower expected production, which confirms our definition of these two

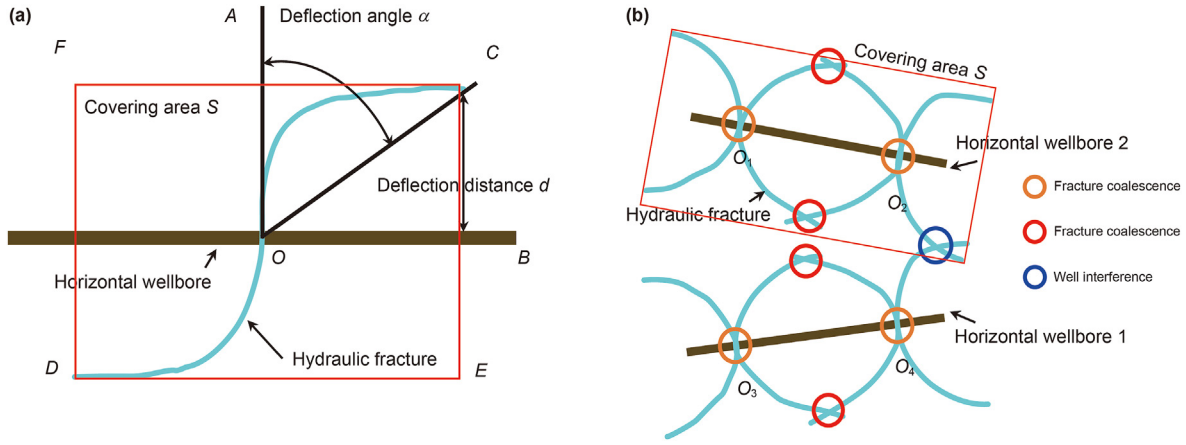

Fig. 5. Schematic diagram of fracturing behavior of (**a**) single fracture and (**b**) multiple fractures.

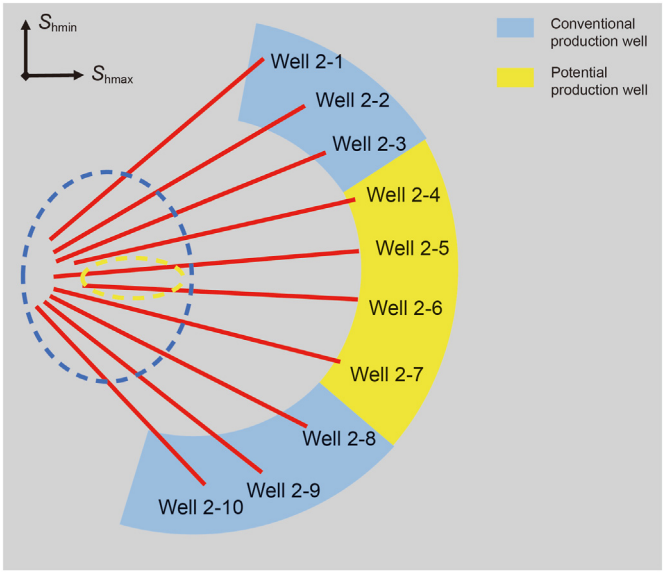

Fig. 6. Locations of ten target non-parallel horizontal wells.

types of non-parallel horizontal wells.

5.2. Optimization of the "heel" section of two wells in the extreme region

Due to the small well spacing, hydraulic fracturing in the "heel" portion of the adjacent wells (marked by the blue circle in Fig. 6) is most likely to cause well interference, especially in the extreme region. Therefore, we choose the "heel" portion of two adjacent wells (marked by the yellow circle in Fig. 6) for optimization design and label them as Wells 3-1 and 3-2 in Fig. 10.

5.2.1. Different fracturing sequences

We first examine the impact of different fracturing sequences. The details of the numerical model are shown in Fig. 10. The model size is 500 m × 400 m × 70 m. The heights of the barrier and the reservoir are 10 and 50 m, respectively. To overcome the rigid boundary conditions, two soft layers are placed along the sides of the model, parallel to the predicted propagation direction of hydraulic fractures. There is one stage with 3 clusters in each well and with a cluster spacing of 20 m. The well spacing is 140 m, and the injection time per stage is 60 min. Other parameters are listed in

Table 3
Deviated angles of ten target wells.

Well No.	2-1	2-2	2-3	2-4	2-5	2-6	2-7	2-8	2-9	2-10
Angle between well and S_{hmin}, degree	42	50	60	72	84	83	72	60	50	42

Table 4
Rock properties and engineering parameters.

Input parameter		Value
Geological parameter	Young's modulus, GPa	33
	Poisson's ratio	0.25
	Porosity, %	8.83
	Permeability, mD	0.1
	Fracture toughness, Pa·m$^{0.5}$	1e6
	Maximum horizontal principal stress, MPa	40
	Minimum horizontal principal stress, MPa	35
	Vertical stress, MPa	45
	Formation pore pressure, MPa	20
	Uniaxial compressive strength, MPa	130
	Tensile strength, MPa	4
Engineering parameter	Injection rate, m^3/min	3
	Injection time for each stage, s	2400

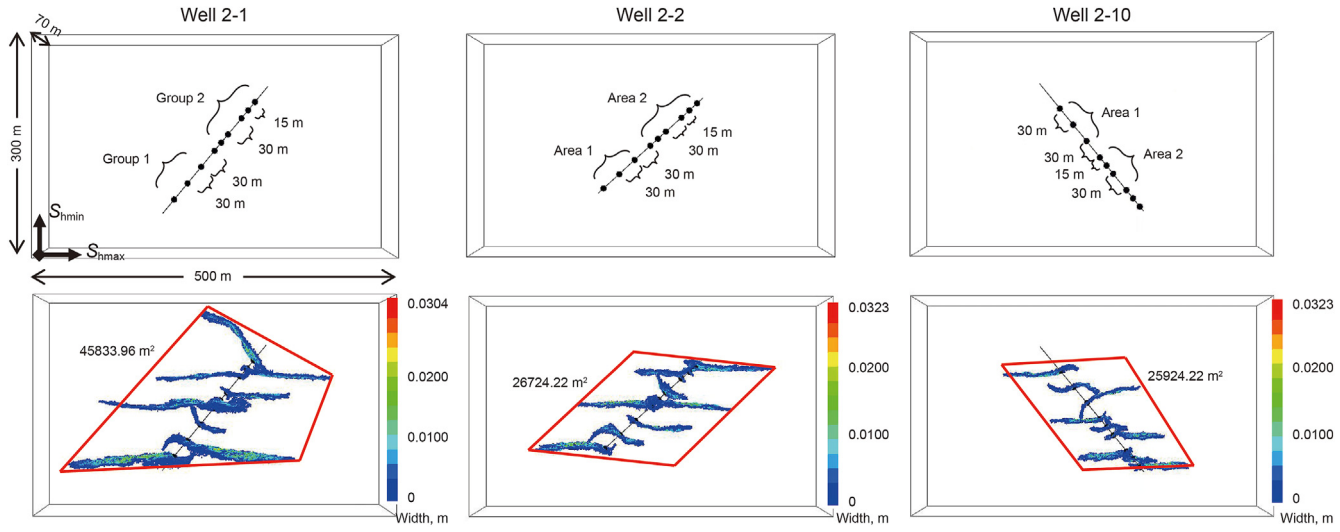

Fig. 7. Fracture morphology of conventional production wells.

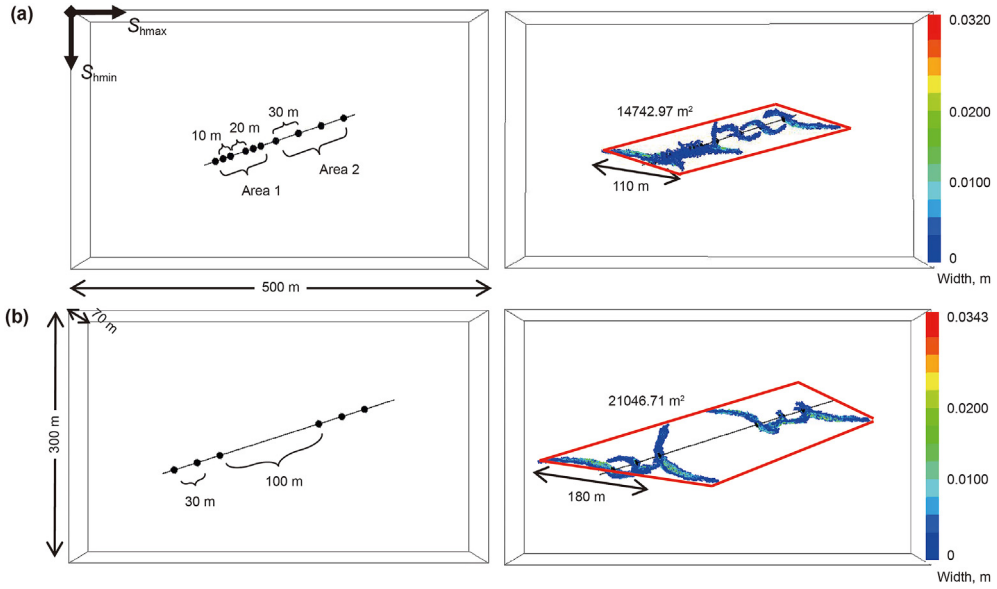

Fig. 8. Comparison of stage arrangement for potential production Well 2-4.

Table 4. Referring to previous studies (Wang and Liu, 2021; Saberhosseini et al., 2021; Zhang et al., 2021), we propose three fracturing sequences, as shown in Fig. 11. In the first design, the initial fractures are aligned, and hydraulic fracturing is performed sequentially, i.e., all three clusters in Well 3-1 are simultaneously fractured and followed by all three clusters in Well 3-2, which is called "Aligned crack & sequential fracturing". In the second design, the initial fractures are aligned, but hydraulic fracturing is performed in a zipper sequence, i.e., in the sequence of ④→①→⑤→②→⑥→③ as shown in Fig. 11, which is called "Aligned crack & zipper fracturing".

The numerical results of the fracture morphology and induced stress evolution under three fracturing sequences are shown in Figs. 12–14. Under sequential fracturing, the middle fracture is perpendicular to the wellbore due to the stress shadowing effect of the fractures on both sides, which is similar to the result of Well 1-7 in Fig. 4(a). Fractures on both sides deflect, with a maximum deflection distance of 25.23 m and a maximum deflection angle of 18.5°. As for induced stress evolution, although stress reversal is seen in some areas around existing fractures, i.e., $S_{yy} > S_{xx}$, after the fracturing of Well 3-1, the affected area does not extend around Well 3-2. Therefore, the fracture morphology of the two wells is similar, and well interference does not occur.

The latter two fracturing sequence designs result in completely different treatment performance. In Fig. 13, "wild goose" type fractures propagate in the first two clusters, either aligned or staggered. However, subsequent fractures ⑤ and ② deflect in the opposite direction, causing well interference. Besides, fractures ④ and ① propagate again interacting with new fractures, increasing the risk of fracture penetration into the barrier, as indicated by red dashed circles in Fig. 13. These propagation behavior can be illustrated by the induced stress evolution in Fig. 14. The propagations of the first two fractures do not affect each other, as shown in Fig. 13. When the third and fourth fractures propagate, the stress distribution is different because the gap between S_{yy} and S_{xx} becomes smaller, and even becomes negative in some areas around cluster ⑤. Therefore,

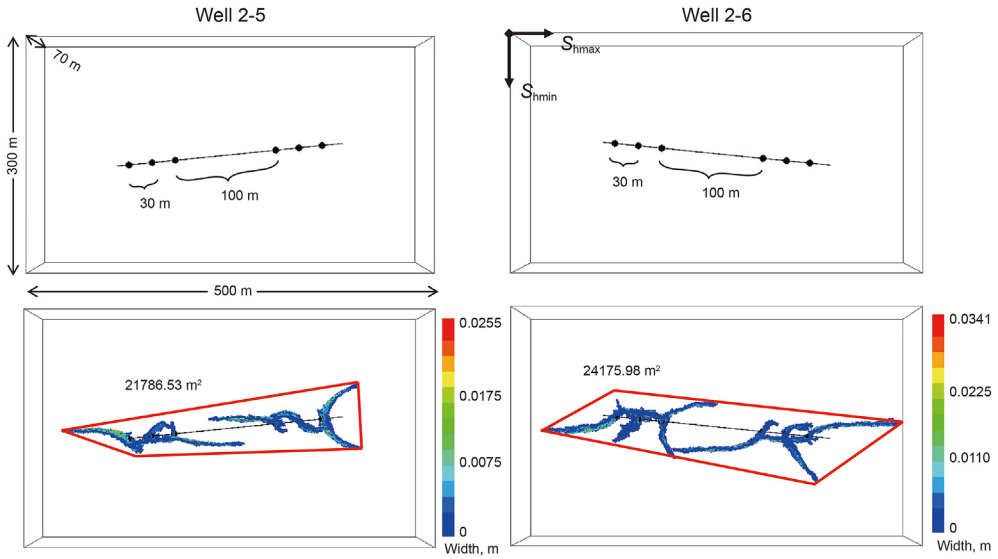

Fig. 9. Final fracture morphology of potential production wells.

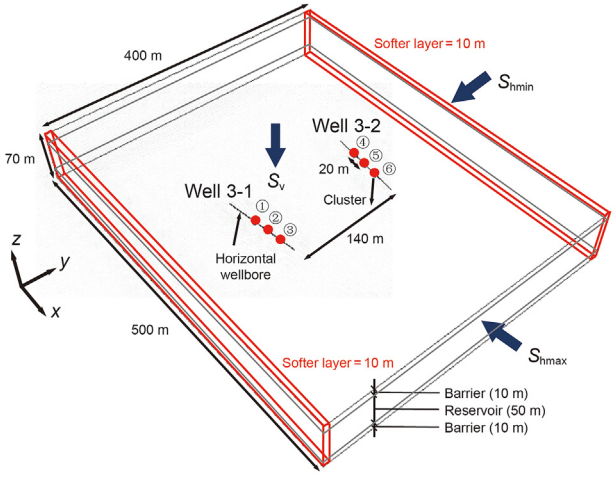

Fig. 10. Numerical model of two adjacent non-parallel horizontal wells.

subsequent fractures deflect reversely under strong stress shadowing effect, and the deflection distance is greater than the previous fractures, resulting in a strong well interference.

In summary, the "Aligned crack & sequential fracturing" design does not induce well interference without excessive stress interference. "Aligned crack & zipper fracturing" design and "Staggered crack & zipper fracturing" design can cause well interference due to the stress shadowing effect in the domain. Based on the above results, simultaneous multi-fracture treatment is a better option to avoid strong well interference.

5.2.2. *Different fracturing techniques*

Two fracturing techniques applied in the field (Leising and Newman, 1993) are discussed. The first technique is to place three clusters in one stage with a uniform large cluster spacing (30 m), defined as LCS. For each cluster, a larger perforation friction is set (Zhang et al., 2021). The second technique is to use a close-cut mode to place eight clusters with a small cluster spacing (8 m) in one stage, defined as SCS. The numerical models of these two fracturing scenarios are illustrated in Fig. 15. Eight cases are simulated using these two techniques, and parameters are listed in Table 5. Injection rate and *in situ* stress condition are considered important factors according to the previous studies (Damjanac et al., 2016; Zhang et al., 2021). Other parameters are the same as listed in Table 4.

A large cluster spacing is applied in Case 1-1 through Case 1-5.

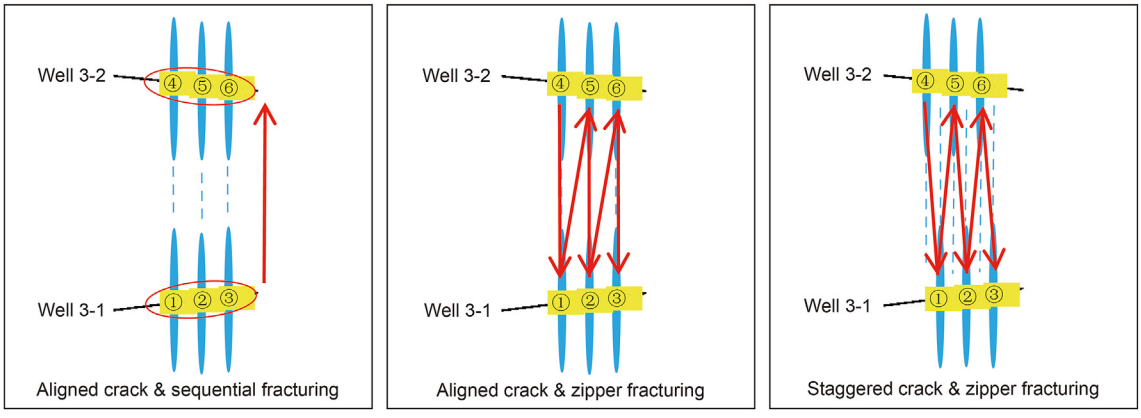

Fig. 11. Scheme diagrams of three different fracturing sequences.

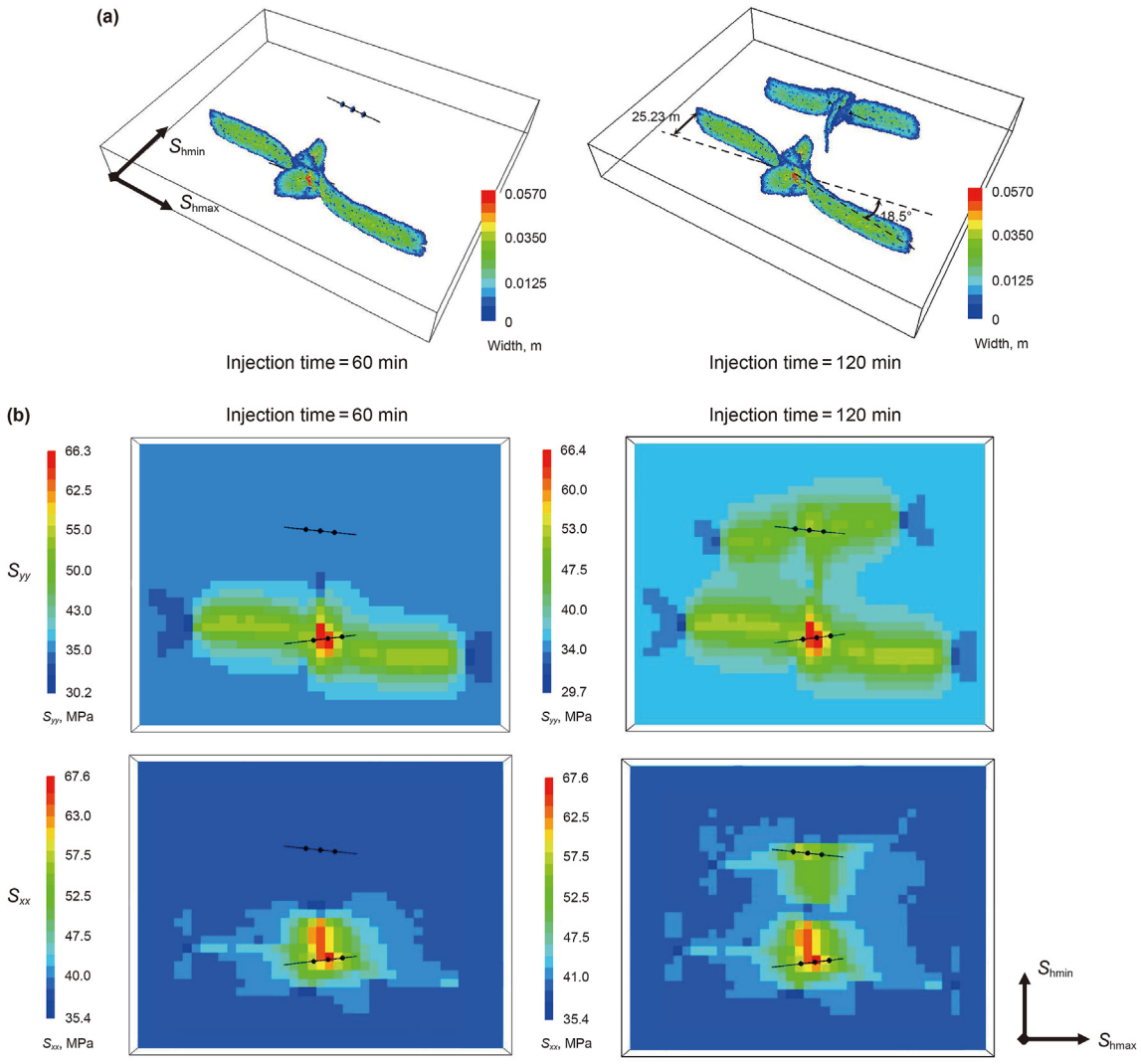

Fig. 12. (**a**) Fracture morphology and (**b**) induced stress evolution of "Aligned crack & sequential fracturing" design.

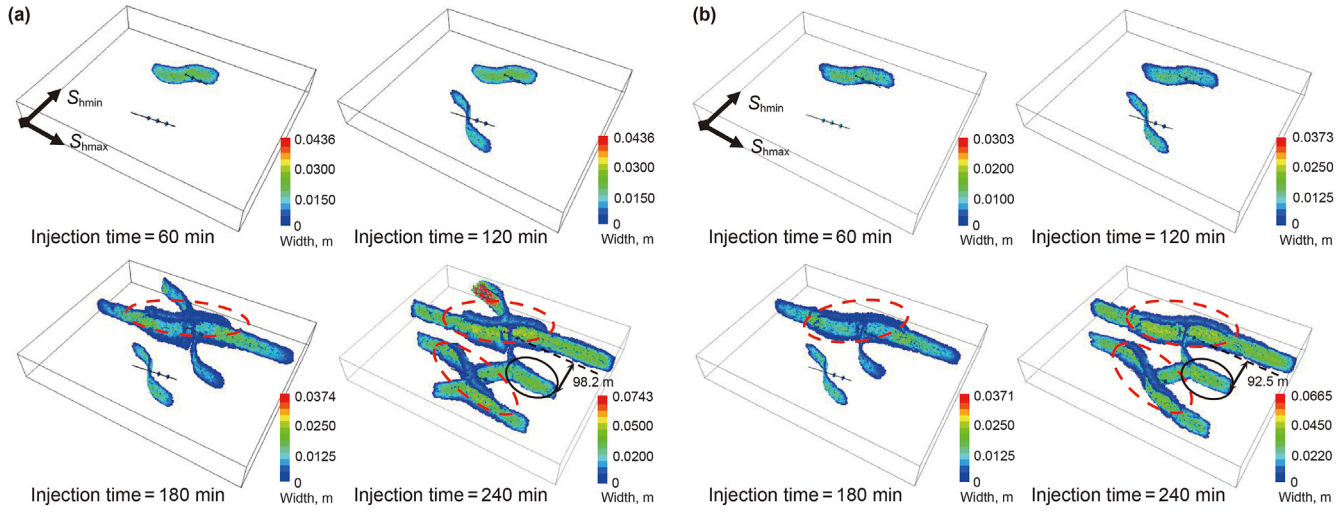

Fig. 13. Fracture morphology of (**a**) "Aligned crack & zipper fracturing" design and (**b**) "Staggered crack & zipper fracturing" design.

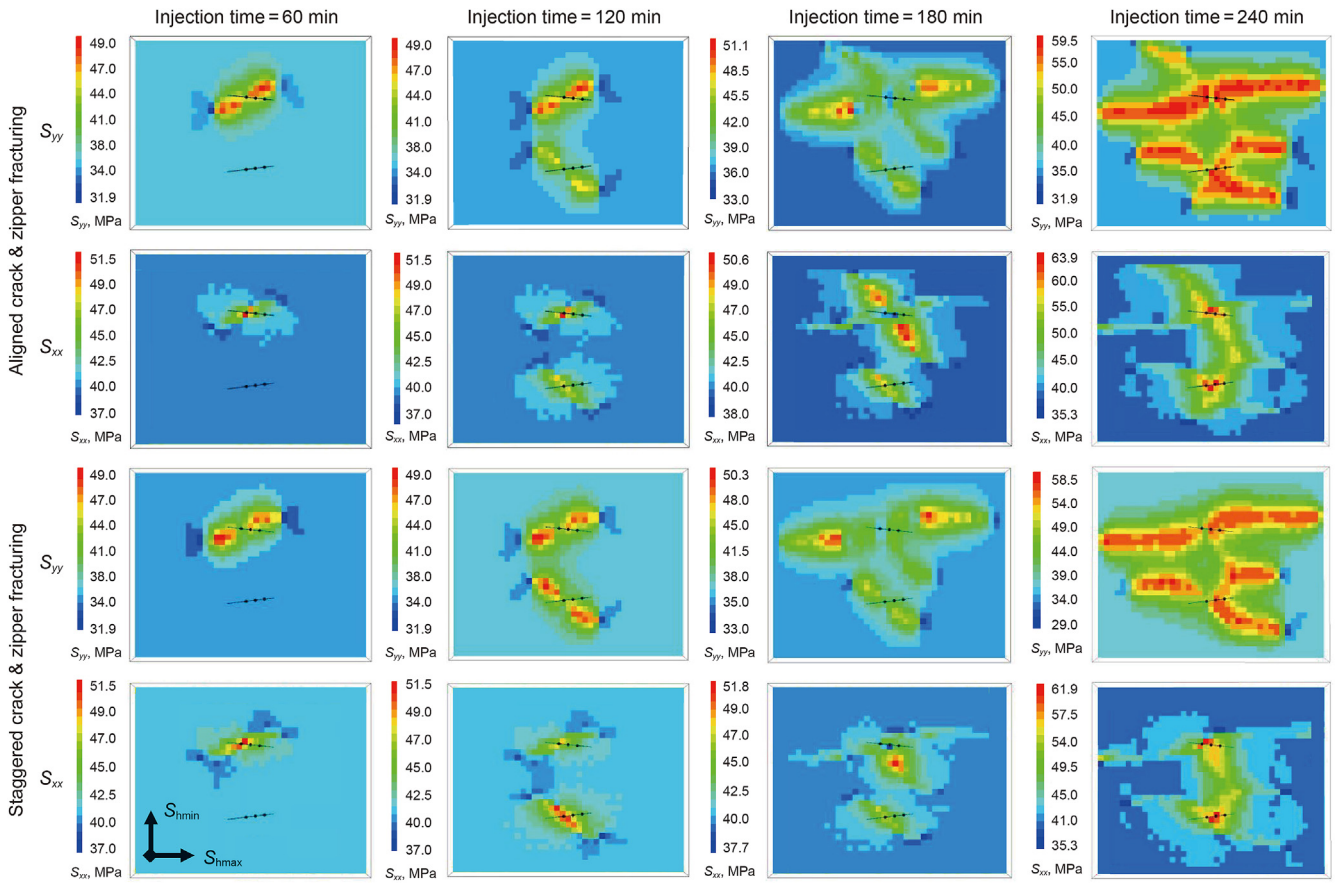

Fig. 14. Induced stress evolution of "Aligned crack & zipper fracturing" design and "Staggered crack & zipper fracturing" design.

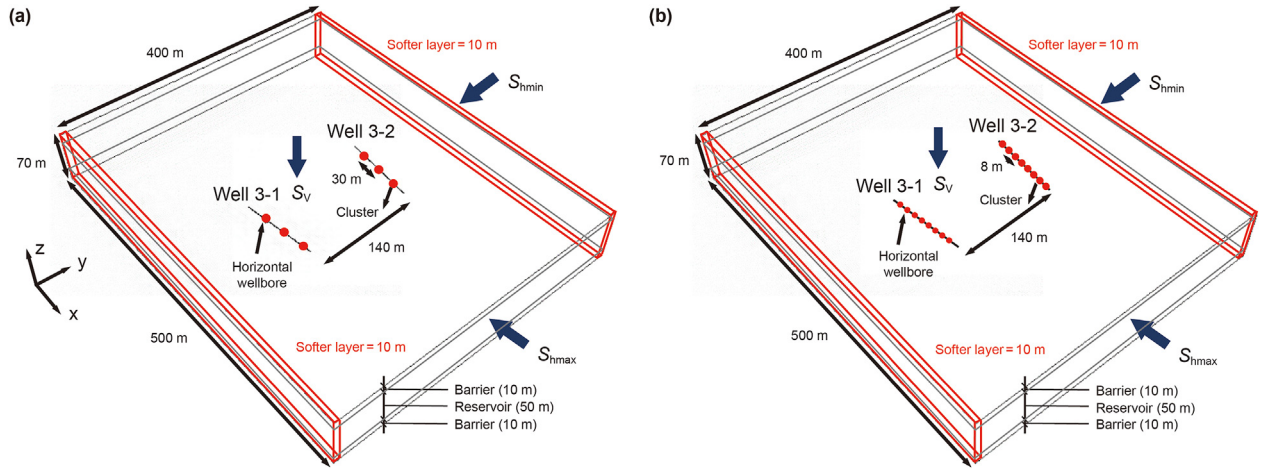

Fig. 15. Numerical models of two fracturing methods, (**a**) large cluster spacing (LCS), and (**b**) small cluster spacing (SCS).

The fracture morphology and the induced stress evolution after fracturing Well 3-2 under different injection rates and initial stresses are displayed in Figs. 16 and 17. The maximum deflection distance (MDD), the maximum deflection angle (MDA), and the covering area (CA) of the two wells in each case are calculated in Table 6.

The influence of different injection rates is investigated in Cases 1-1, 1-2, and 1-3. As can be seen in Fig. 16, the fracture morphology of the two wells looks similar at 6 and 9 m^3/min, respectively. Due to the large injection rate, a larger fracture aperture is shown in Case 1-2. In Case 1-3, the fluid pressure in the fracture is large enough to allow Well 3-2 to have a larger covering area with a smaller deflection angle and a larger deflection distance, but subsequent stress shadowing prevents the following propagation of fractures in Well 3-1. This is confirmed in Fig. 17. At a low small injection rate, the induced stress around Well 3-2 does not affect the stress distribution around Well 3-1, while the large injection rate can cause negative stress shadowing on the remaining unfractured wells.

Table 5
Input parameters for the designed numerical cases.

Case No.	Well No.	S_{hmax}, Pa	S_{hmin}, MPa	Stress differential, MPa	Injection rate, m^3/min	Fracturing technique
Case 1-1	Well 3-1	35	30	5	6	LCS
	Well 3-2	35	30	5	6	LCS
Case 1-2	Well 3-1	35	30	5	9	LCS
	Well 3-2	35	30	5	9	LCS
Case 1-3	Well 3-1	35	30	5	12	LCS
	Well 3-2	35	30	5	12	LCS
Case 1-4	Well 3-1	35	32	3	12	LCS
	Well 3-2	35	32	3	12	LCS
Case 1-5	Well 3-1	35	33	2	12	LCS
	Well 3-2	35	33	2	12	LCS
Case 2-1	Well 3-1	35	30	5	14	SCS
	Well 3-2	35	30	5	14	SCS
Case 2-2	Well 3-1	35	32	3	14	SCS
	Well 3-2	35	32	3	14	SCS
Case 2-3	Well 3-1	35	33	2	14	SCS
	Well 3-2	35	33	2	14	SCS

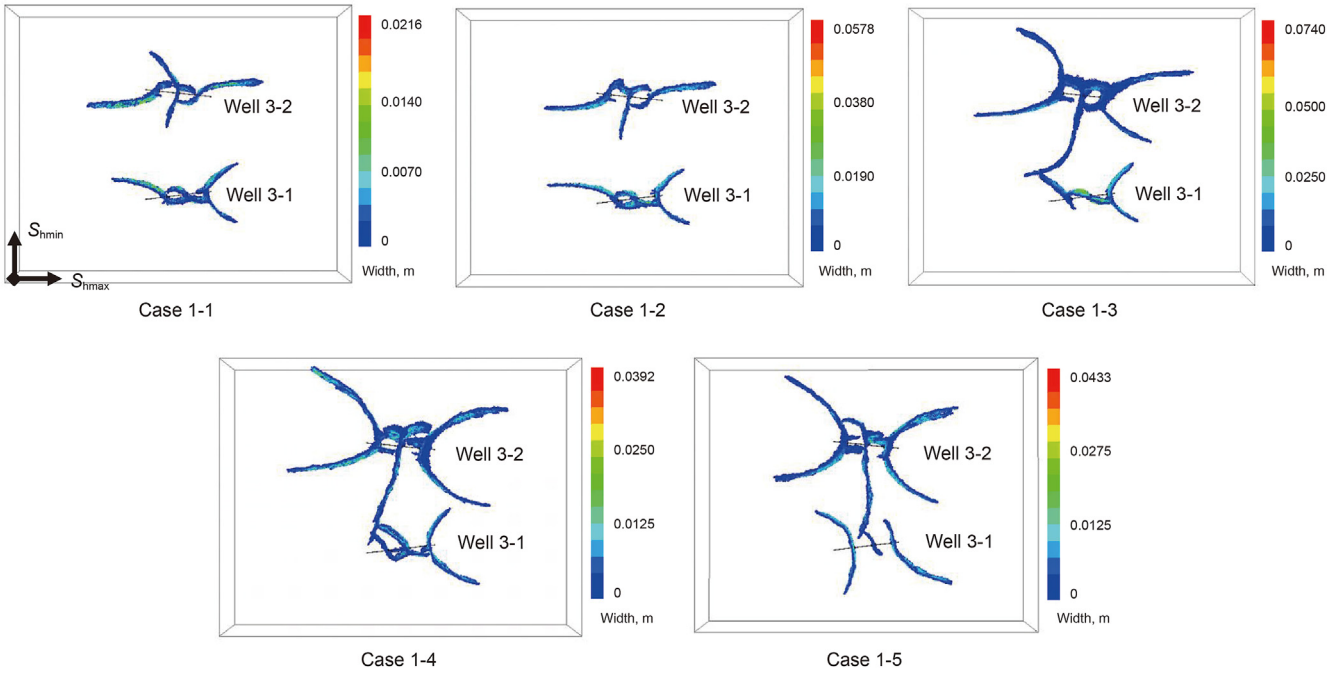

Fig. 16. Fracture morphology of Case 1-1 to Case 1-5.

We then investigate the effect of different stress differentials in Cases 1-3, 1-4, and 1-5. In Case 1-4, deflection of the middle fracture still occurs after propagation, resulting in similar treatment performance to Case 1-3. However, Case 1-5 has the smallest initial stress differential of 2 MPa, the middle fracture propagates mostly parallel to the S_{hmin} direction because the stress shadowing of the fractures on both sides is dominant compared to the small stress difference. Therefore, only the middle fracture of Well 3-1 is hindered, and fractures on both ends can propagate perpendicular to the wellbore under the stress shadowing effect of the middle fracture to achieve a larger covering area for an ideal stimulation performance.

Next, Cases 2-1, 2-2, and 2-3 are simulated under small cluster spacing. Based on the analysis of Case 1-1 through Case 1-5, a large injection rate of 14 m^3/min is used. The effect of stress differential is also considered. In Cases 2-1, 2-2, and 2-3, the initial stress differences are 5, 3, and 2 MPa, respectively. The numerical results are shown in Figs. 18 and 19, and Table 6. Due to the small cluster spacing, all fractures in each case merge together after initiation, forming a "fracture core" with a large aperture in the center. In Case 2-1, the stress difference is large, which is easy to cause planar fractures with small deflection distance and large deflection angle, and a sharp deflection may result in a small fracture core and covering area. With the decrease in stress differential, the deflection angle decreases, while the deflection distance and covering area increase with the increase in fracture branches. With the smallest stress differential (2 MPa), fracture branches of the two wells can propagate into the half region of the other well and communicate in the middle. For induced stress, the affected area of one well cannot extend into the other half region because of the

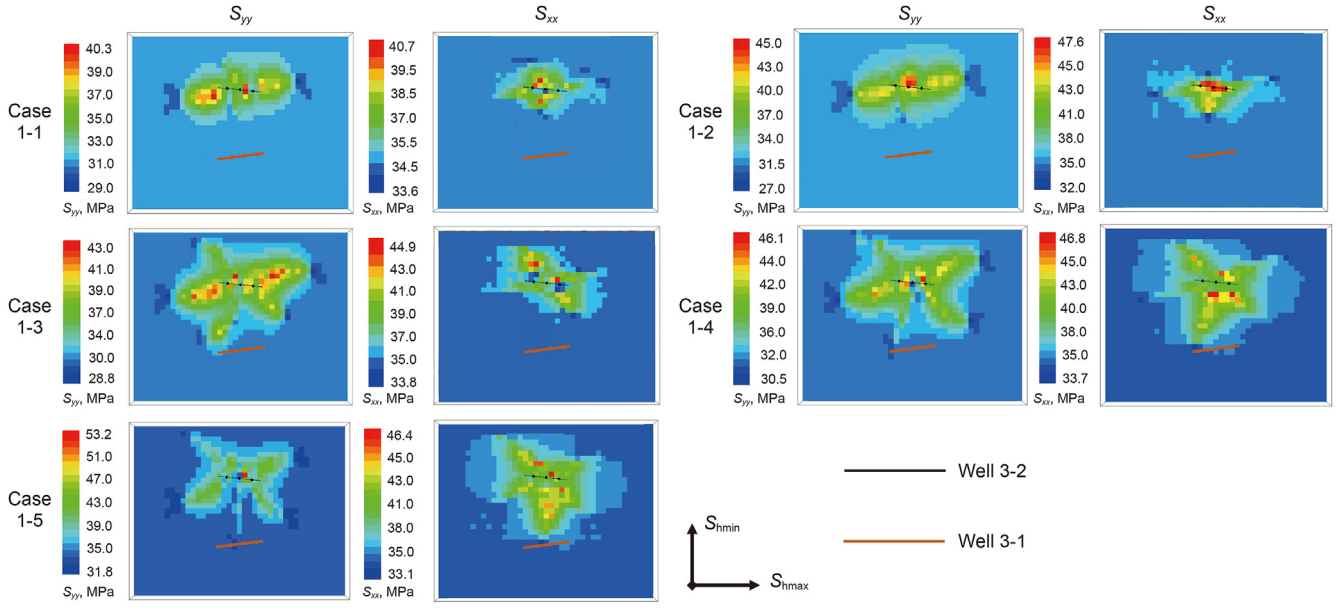

Fig. 17. Induced stress evolution of Case 1-1 to Case 1-5 after Well 3-2 is fractured.

Table 6
Evaluation index values of Case 1-1 to Case 1-5 and Case 2-1 to Case 2-3.

Case No.	Well 3-1			Well 3-2		
	MDD, m	MDA, degree	CA, m^2	MDD, m	MDA, degree	CA, m^2
Case 1-1	39.3	62.1	7,698.3	23.6	67.1	15,608.0
Case 1-2	49.5	67.0	8,151.2	27.5	74.4	10,189.0
Case 1-3	39.1	38.5	6,473.0	99.7	47.7	44,571.1
Case 1-4	61.5	34.2	9,541.4	100.8	45.0	59,112.4
Case 1-5	67.8	28.8	14,724.2	89.6	43.2	48,179.2
Case 2-1	52.4	46.8	15,754.8	52.6	50.0	19,087.6
Case 2-2	82.2	36.9	23,048.0	85.5	30.0	23,773.3
Case 2-3	92.1	33	31,845.1	98.7	27.9	33,803.7

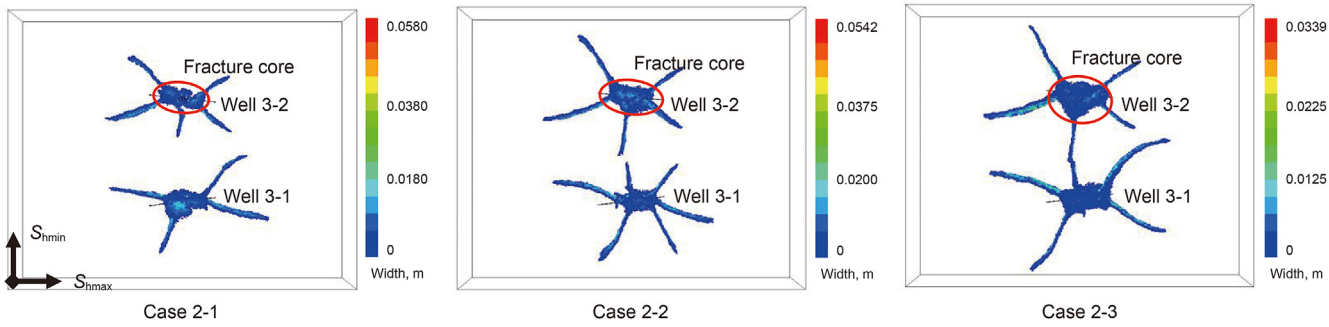

Fig. 18. Fracture morphology of Case 2-1 to Case 2-3.

small injection rate per cluster.

In summary, two different fracturing techniques exhibit different behavior in the sectorial well-factory. Under a large cluster spacing design, increasing injection rate can promote fracture propagation and increase the stimulated reservoir volume (SRV). The deflection of the middle fracture in the pre-fractured well can hinder the propagation of subsequent fractures due to strong stress shadowing effect. However, when the stress differential is small enough, the stress shadowing effect contributes to an ideal treatment performance. Under a small cluster spacing design, the induced stress evolution area of each well does not extend to the other half region too much. Reducing the stress differential can increase the deflection distance while reducing the deflection angle. Simultaneous multi-fracture treatment results in a fracture core that increases with decreasing stress differential.

6. Discussion

The sectorial well-factory is an innovative model that considers large-scale production and environmental protection. Critical issues in hydraulic fracturing in the sectorial well-factory are fracture deflection and subsequent well interference. We have tried to

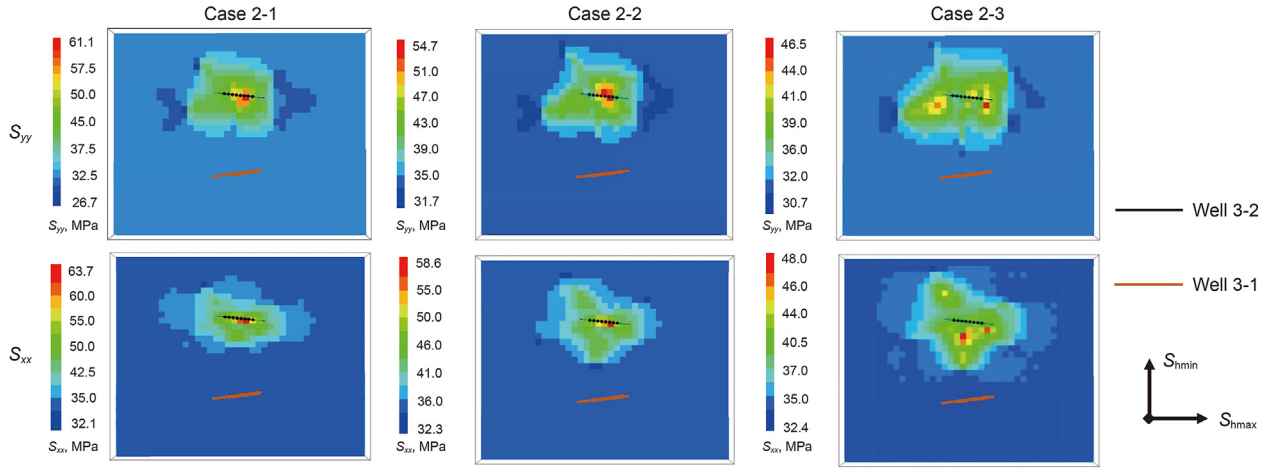

Fig. 19. Induced stress evolution of Case 2-1 to Case 2-3.

tackle these issues with different designs and a deeper understanding is needed to guide the well and completion design for this configuration.

Depending on the well type, a larger covering area can be achieved successfully through a "gradual" or "sparse" stage arrangement. Fracture coalescence between clusters and stages can be beneficial under certain conditions. Well interference is likely to occur at large injection rates. However, in Case 1-5, we see a representation of an ideal stimulation, where only the central fracture is hindered by the planar fracture under a small stress differential. Therefore, if the middle cluster of the post-fractured well is removed and the middle fracture is allowed to penetrate the remaining clusters, the fractures will not communicate under the stress shadowing effect. In that case, the entire stage arrangement of the two wells can be seen as an "oversized" staggered arrangement, which can lead to over capitalization.

This work is mainly focused on the feasibility of initial fracturing in the original reservoir. In reality, the stress differential is more complicated which can affect the fracturing sequence decision and the induced stress results will be different from model prediction. At the same time, natural fractures should be considered, as they can interact with hydraulic fractures. Other engineering parameters such as fracturing fluid viscosity, proppant concentration, and leak-off coefficient should also be taken into account. At last, as shown in Fig. 14, the stress distribution in the reservoir is changed significantly, which results in stress reversal where fractures are present. Furthermore, if a refracturing is conducted sequentially in the same reservoir under the same layout of the sectorial well-factory, the deflection and well-interference will be improved theoretically, which is a promising part for our future work.

7. Conclusions

In this paper, we develop a new numerical model of the sectorial well-factory based on three-dimensional lattice method and investigate its feasibility of hydraulic fracturing. Evaluation indexes are proposed scientifically and comprehensive optimization designs are carried out for fracture propagation, including different stage arrangements, fracturing sequences, and fracturing techniques with various injection rates and *in situ* stress conditions. The resulting fracture morphology is analyzed considering well interference and stress shadowing. Optimization guidance can be provided for the sectorial well-factory from the following conclusions.

(1) Compared with parallel well-factory, the main issues of the sectorial well-factory are the fracture deflection driven by initial stresses and well interference. Increasing horizontal stress difference will sharpen the deflection and induce planar fracture propagation.
(2) For multi-stage fracturing of a single well in the sectorial well-factory, "gradual" and "sparse" stage arrangements are recommended according to well types to optimize stimulation performance.
(3) When performing simultaneous multi-fracture treatment in a sectorial well-factory, a large injection rate is recommended as it improves fracture deflection, but the resulting stress shadowing effect often prevents subsequent fracture propagation.
(4) For areas with small stress differentials, large injection rates with an "oversized" staggered stage arrangement can cause positive stress shadowing effect for optimal stimulation performance.

Declaration of competing interest

The authors declare that they have no known competing financial interests or personal relationships that could have appeared to influence the work reported in this paper.

Acknowledgments

This research is funded by the National Natural Science Foundation of China (42077247, 52104029) and the Fundamental Research Funds for the Central Universities.

References

Al-Khamis, M., Ozkan, E., Raghavan, R., 2003. Analysis of interference tests with horizontal wells. In: SPE Annual Technical Conference and Exhibition. https://doi.org/10.2118/84292-MS.
Bakhshi, E., Rasouli, V., Ghorbani, A., et al., 2019. Lattice numerical simulations of lab-scale hydraulic fracture and natural interface interaction. Rock Mech. Rock Eng. 52 (5), 1315–1337. https://doi.org/10.1007/s00603-018-1671-2.
Benouadah, N., Djabelkhir, N., Song, X., et al., 2021. Simulation of competition between transverse notches versus axial fractures in open hole completion hydraulic fracturing. Rock Mech. Rock Eng. 54 (5), 2249–2265. https://doi.org/10.1007/s00603-021-02378-2.
Bourdin, B., Chukwudozie, C., Yoshioka, K., 2012. A variational approach to the numerical simulation of hydraulic fracturing. In: SPE Annual Technical Conference and Exhibition. https://doi.org/10.2118/159154-MS.
Chen, X., Li, Y., Zhao, J., et al., 2018. Numerical investigation for simultaneous growth of hydraulic fractures in multiple horizontal wells. J. Nat. Gas Sci. Eng. 51,

44–52. https://doi.org/10.1016/j.jngse.2017.12.014.
Damjanac, B., Cundall, P.A., 2016. Application of distinct element methods to simulation of hydraulic fracturing in naturally fractured reservoirs. Comput. Geotech. 71, 283–294. https://doi.org/10.1016/j.compgeo.2015.06.007.
Damjanac, B., Detournay, C., Cundall, P.A., 2016. Application of particle and lattice codes to simulation of hydraulic fracturing. Comput. Part. Mech 3 (2), 249–261. https://doi.org/10.1007/s40571-015-0085-0.
Daneshy, A., Au-Yeung, J., Thompson, T., et al., 2012. Fracture shadowing: a direct method for determining of the reach and propagation pattern of hydraulic fractures in horizontal wells. In: SPE Hydraulic Fracturing Technology Conference. https://doi.org/10.2118/151980-MS.
Detournay, C., Damjanac, B., Torres, M., et al., 2022. Heat advection and forced convection in a lattice code – implementation and geothermal applications. Rock Mech. Bull. 1 (1), 100004. https://doi.org/10.1016/j.rockmb.2022.100004.
Detournay, E., 2016. Mechanics of hydraulic fractures. Annu. Rev. Fluid Mech. 48, 311–339. https://doi.org/10.1146/annurev-fluid-010814-014736.
Dontsov, E.V., 2016. An approximate solution for a penny-shaped hydraulic fracture that accounts for fracture toughness, fluid viscosity and leak-off. R. Soc. Open Sci. 3 (12), 160737. https://doi.org/10.1098/rsos.160737.
Dontsov, E.V., 2022. Analysis of a constant height hydraulic fracture driven by a power-law fluid. Rock Mech. Bull. 1 (1), 100003. https://doi.org/10.1016/j.rockmb.2022.100003.
Duan, K., Li, Y., Yang, W., 2021. Discrete element method simulation of the growth and efficiency of multiple hydraulic fractures simultaneously-induced from two horizontal wells. Geomech Geophys. Geo-Energy. Geo-Resour. 7 (1), 1–20. https://doi.org/10.1007/s40948-020-00196-4.
Feng, Y., Jones, J.F., Gray, K.E., 2016. A review on fracture-initiation and -propagation pressures for lost circulation and wellbore strengthening. SPE Drill. Complet. 31 (2), 134–144. https://doi.org/10.2118/181747-PA.
Feng, Y., Li, X., Gray, K.E., 2017. Development of a 3D numerical model for quantifying fluid-driven interface debonding of an injector well. Int. J. Greenh. Gas Control 62, 76–90. https://doi.org/10.1016/j.ijggc.2017.04.008.
LaFollette, R.F., Holcomb, W.D., 2011. Practical data mining: lessons learned from the Barnett Shale of North Texas. In: SPE Hydraulic Fracturing Technology Conference. https://doi.org/10.2118/140524-MS.
Leising, L.J., Newman, K.R., 1993. Coiled-tubing drilling. SPE Drill. Complet. 8 (4), 227–232. https://doi.org/10.2118/24594-PA.
Liu, Q., Tian, S., Yu, W., et al., 2020. A semi-analytical model for simulation of multiple vertical wells with well interference. J. Petrol. Sci. Eng. 195, 107830. https://doi.org/10.1016/j.petrol.2020.107830.
Liu, X., Rasouli, V., Guo, T., et al., 2020. Numerical simulation of stress shadow in multiple cluster hydraulic fracturing in horizontal wells based on lattice modelling. Eng. Fract. Mech. 238, 1072–1078. https://doi.org/10.1016/j.engfracmech.2020.107278.
Molina, O., Zeidouni, M., 2017. Analytical approach to determine the degree of interference between multi-fractured horizontal wells. In: SPE Europec Featured at 79th EAGE Conference and Exhibition. https://doi.org/10.2118/185765-MS.
Saberhosseini, S.E., Chen, Z., Sarmadivaleh, M., 2021. Multiple fracture growth in modified zipper fracturing. Int. J. GeoMech. 21 (7). https://doi.org/10.1061/(ASCE)GM.1943-5622.0002040.
Shan, Q., Zhang, R., Jiang, Y., 2021. Complexity and tortuosity hydraulic fracture morphology due to near-wellbore nonplanar propagation from perforated horizontal wells. J. Nat. Gas Sci. Eng. 89, 103884. https://doi.org/10.1016/j.jngse.2021.103884.
Sobhaniaragh, B., Trevelyan, J., Mansur, W.J., et al., 2017. Numerical simulation of MZF design with non-planar hydraulic fracturing from multi-lateral horizontal wells. J. Nat. Gas Sci. Eng. 46, 93–107. https://doi.org/10.1016/j.jngse.2017.07.005.
Tang, H., Chai, Z., Yan, B., et al., 2017. Application of multi-segment well modeling to simulate well interference. In: SPE/AAPG/SEG Unconventional Resources Technology Conference. https://doi.org/10.15530/URTEC-2017-2668100.
Tang, J., Wu, K., Zuo, L., et al., 2019. Investigation of rupture and slip mechanisms of hydraulic fracture in multiple-layered formation. SPE J. 24 (5), 2292–2307. https://doi.org/10.2118/197054-PA.
Tang, X., Rutqvist, J., Hu, M., et al., 2019. Modeling three-dimensional fluid-driven propagation of multiple fractures using TOUGH-FEMM. Rock Mech. Rock Eng. 52 (2), 611–627. https://doi.org/10.1007/s00603-018-1715-7.
Thompson, L.G., 2018. Horizontal well fracture interference – Semi-analytical modeling and rate prediction. J. Petrol. Sci. Eng. 160, 465–473. https://doi.org/10.1016/j.petrol.2017.10.002.
Vidma, K., Abivin, P., Fox, D., et al., 2018. Fracture geometry control technology prevents well interference in the Bakken. In: SPE Hydraulic Fracturing Technology Conference and Exhibition. https://doi.org/10.2118/194333-MS.
Wang, L., Duan, K., Zhang, Q., et al., 2022. Study of the dynamic fracturing process and stress shadowing effect in granite sample with two holes based on SCDA fracturing method. Rock Mech. Rock Eng. 55 (3), 1537–1553. https://doi.org/10.1007/s00603-021-02728-0.
Wang, X., Zhang, F., Yin, Z., et al., 2022a. Numerical investigation of refracturing with/without temporarily plugging diverters in tight reservoirs. Petrol. Sci. 19 (5), 2210–2226. https://doi.org/10.1016/j.petsci.2022.05.006.
Wang, X., Zhang, F., Tang, M., et al., 2022b. Effect of stress shadow caused by multistage fracturing from multiple well pads on fracture initiation and near-wellbore propagation from infill wells. SPE J. 27 (1), 204–225. https://doi.org/10.2118/208577-PA.
Wang, X., Tang, M., Du, X., et al., 2022c. Three-dimensional experimental and numerical investigations on fracture initiation and propagation for oriented limited-entry perforation and helical perforation. Rock Mech. Rock Eng. 1–26. https://doi.org/10.1007/s00603-022-03069-2.
Wang, X., Zhang, F., Tang, M., et al., 2023. Numerical investigation of hydraulic fracture deflection in large-angle oblique horizontal wells with staged multi-cluster fracturing. Geoenergy. Sci. Eng. 222, 211436. https://doi.org/10.1016/j.geoen.2023.211436.
Wang, Y., Liu, X., 2021. Stress-dependent unstable dynamic propagation of three-dimensional multiple hydraulic fractures with improved fracturing sequences in heterogeneous reservoirs: numerical cases study via poroelastic effective medium model. Energy Fuel. 35 (22), 18543–18562. https://doi.org/10.1021/acs.energyfuels.1c03132.
Wang, Z., Yang, L., Gao, R., et al., 2022. Numerical analysis of zipper fracturing using a non-planar 3D fracture model. Front. Earth Sci. 10, 181–192. https://doi.org/10.3389/feart.2022.808183.
Wei, C., L, Y., Deng, Y., et al., 2022. Analytical well-test model for hydraulically fractured wells with multiwell interference in double porosity gas reservoirs. J. Nat. Gas Sci. Eng. 103, 104624. https://doi.org/10.1016/j.jngse.2022.104624.
Wu, K., Olson, J.E., 2015. Simultaneous multifracture treatments: fully coupled fluid flow and fracture mechanics for horizontal wells. SPE J. 20 (2), 337–346. https://doi.org/10.2118/167626-PA.
Wu, K., Olson, J.E., 2016. Mechanisms of simultaneous hydraulic-fracture propagation from multiple perforation clusters in horizontal wells. SPE J. 21 (3), 1000–1008. https://doi.org/10.2118/178925-PA.
Wu, K., Wu, B., Yu, W., 2018. Mechanism analysis of well interference in unconventional reservoirs: insights from fracture-geometry simulation between two horizontal wells. SPE Prod. Oper. 33 (1), 12–20. https://doi.org/10.2118/186091-PA.
Wutherich, K., Xu, L., Walker, K., et al., 2013. Quantifying the effect of drilling azimuth in shale gas reservoirs. SPE Eastern Regional Meeting. https://doi.org/10.2118/165672-MS.
Xavier Fiallos, M., Yu, W., Ganjdanesh, R., et al., 2019. Modeling interwell interference due to complex fracture hits in eagle ford using EDFM. In: International Petroleum Technology Conference. https://doi.org/10.2523/IPTC-19468-MS.
Yang, F., Britt, L.K., Dunn-Norman, S., 2016. Performance comparison of transversely and longitudinally fractured horizontal wells over varied reservoir permeability. SPE J. 21 (5), 1537–1553. https://doi.org/10.2118/173331-PA.
Yoshioka, K., Mollaali, M., Kolditz, O., 2021. Variational phase-field fracture modeling with interfaces. Comput. Methods Appl. Mech. Eng. 384, 1139–1151. https://doi.org/10.1016/j.cma.2021.113951.
Yu, W., Xu, Y., Weijermars, R., et al., 2017. Impact of well interference on shale oil production performance: a numerical model for analyzing pressure response of fracture hits with complex geometries. In: SPE Hydraulic Fracturing Technology Conference and Exhibition. https://doi.org/10.2118/184825-MS.
Yu, W., Xu, Y., Weijermars, R., et al., 2018. A numerical model for simulating pressure response of well interference and well performance in tight oil reservoirs with complex-fracture geometries using the fast embedded-discrete-fracture-model method. SPE Reservoir Eval. Eng. 21 (2), 489–502. https://doi.org/10.2118/184825-PA.
Zhang, F., Wang, X., Tang, M., et al., 2021. Numerical investigation on hydraulic fracturing of extreme limited entry perforating in plug-and-perforation completion of shale oil reservoir in Changqing Oilfield, China. Rock Mech. Rock Eng. 54 (6), 2925–2941. https://doi.org/10.1007/s00603-021-02450-x.
Zhao, X., Jin, F., Liu, X., et al., 2022. Numerical study of fracture dynamics in different shale fabric facies by integrating machine learning and 3-D lattice method: a case from Cangdong Sag, Bohai Bay basin, China. J. Petrol. Sci. Eng. https://doi.org/10.1016/j.petrol.2022.110861.
Zinn, C., Blood, D.R., Morath, P., 2011. Evaluating the impact of wellbore azimuth in the marcellus shale. In: SPE Eastern Regional Meeting. https://doi.org/10.2118/149468-MS.